Carbon materials as additives to the OER catalysts: RRDE study of carbon corrosion at high anodic potentials

Ivan Filimonenkov, Corinne Bouillet, Gwénaëlle Kerangueven, Pavel A. Simonov, Galina A. Tsirlina, Elena Savinova

Version of Record: https://www.sciencedirect.com/science/article/pii/S0013468619315257
Manuscript_6ad80645fc8604090f910c08db38b1b6

Carbon materials as additives to the OER catalysts: RRDE study of carbon corrosion at high anodic potentials

Ivan S. Filimonenkov[a,b,*], Corinne Bouillet[c], Gwénaëlle Kéranguéven[b], Pavel A. Simonov[d], Galina A. Tsirlina[a], Elena R. Savinova[b]

[a] *Department of Electrochemistry, Faculty of Chemistry, Lomonosov Moscow State University, 1 str. 3 Leninskie Gory, 119991 Moscow, Russia*

[b] *Institut de Chimie et Procédés pour l'Énergie, l'Environnement et la Santé, UMR 7515 du CNRS-ECPM, 25 rue Becquerel, 67087 Strasbourg Cedex 2, France*

[c] *Institut de Physique et Chimie des Matériaux de Strasbourg, DSI, 23 rue du Lœss, 67034 Strasbourg, France*

[d] *Boreskov Institute of Catalysis, 5 Prospekt Lavrentieva, 630090 Novosibirsk, Russia*

Abstract

Carbon materials are widely applied as conductive additives in studies of the oxygen evolution reaction (OER) in alkaline media catalyzed by transition metal oxides. In this work we investigate the anodic behavior of three representative carbon materials: furnace black (Vulcan XC-72R), acetylene black, and pyrolytic carbon of the Sibunit family (Sibunit-152), in 1 M NaOH at high potentials (ranging from the OER onset and up to *ca*. 2 V vs. RHE) in the time span from several minutes to several hours. We apply the rotating ring-disk electrode (RRDE) to separate the OER current from the carbon corrosion current. We then use transmission electron microscopy (TEM) to visualize changes in the carbon

* Corresponding author. Department of Electrochemistry, Faculty of Chemistry, Lomonosov Moscow State University, 1 str. 3 Leninskie Gory, 119991 Moscow, Russia
E-mail addresses: filimonenkov@elch.chem.msu.ru, ivan.filimonenkov@etu.unistra.fr (I.S. Filimonenkov).

morphology resulting from corrosion. Finally, we study the OER performance of composite electrodes comprising carbon materials mixed with a $La_{0.5}Sr_{0.5}Mn_{0.5}Co_{0.5}O_{3-\delta}$ perovskite OER catalyst, and discuss possible influence of the oxide on the carbon corrosion.

Keywords: Carbon materials, Oxygen evolution reaction (OER), Rotating Ring-Disk Electrode (RRDE), Carbon corrosion, Lifetime

1. Introduction

Carbon materials are widely used as catalysts or catalyst supports in electrochemical energy conversion and storage systems [1]. High electronic conductivity, low cost as well as structural and morphological diversity urge their utilization as additives for improving the electronic conductivity of poorly-conductive electrocatalysts, for instance, metals oxides. Recent years have evidenced significant increase in the interest towards transition metal oxides as catalysts of the oxygen evolution reaction (OER) in alkaline media [2–8]. While corrosion instability of carbon materials under the OER conditions usually prevents industry from considering them as additives in the anodes of water electrolysis systems, vast number of model studies of the OER in alkaline media (see Refs. [2,7] and references therein) is performed with transition metal oxides either mixed with or supported on carbon materials. Indeed, addition of carbon materials to poorly conductive oxides has proven to strongly enhance the surface utilization and thus the OER activity of the latter [3,4,9]. Besides, recent studies consider heteroatom-doped and undoped carbons as a potential alternative to the state-of-the-art OER electrocatalysis [10–12].

One should keep in mind however that anodic degradation of carbon materials may not only decrease the extent of the metal oxide utilization during the OER, but also lead to an uncertainty in the OER activity determination, if the latter is calculated from the total

current neglecting the corrosion contribution. Thus, investigation of the carbon corrosion is essential for accessing the OER performance of the catalyst/carbon compositions. While corrosion of carbon materials in aqueous acidic electrolytes (see Refs. [13–17] and references therein) as well as in membrane-electrode assemblies of proton exchange membrane fuel cells (see Refs. [18–21] and references therein) has been extensively investigated, only a few studies have been performed in alkaline solutions [22–24].

The objective of this work is to investigate corrosion resistance of carbon materials, either when used alone or within oxide/carbon compositions, in 1 M NaOH solution, in the potential interval from the OER onset and up to *ca*. 2 V vs. RHE, and in the time span from several minutes to several hours. We have chosen to study an OER catalyst, a $La_{0.5}Sr_{0.5}Mn_{0.5}Co_{0.5}O_{3-\delta}$ (LSMC) perovskite, whose activity is strongly enhanced upon carbon addition [25], and three representative carbon materials with grossly different morphology and microstructure: furnace black (Vulcan XC-72R), acetylene black, and pyrolytic carbon of the Sibunit family (Sibunit-152). We apply the rotating ring-disk electrode (RRDE) for the quantitative determination of the OER current efficiency and for the calculation of the corrosion currents. Transmission electron microscopy (TEM) is then used to visualize morphological evolution resulting from carbon corrosion. We estimate the lifetime of each carbon material under the OER conditions and attempt to correlate corrosion resistance with their microstructure and their OER activity. We then study the OER on LSMC/C electrodes to elucidate possible influence of the oxide on the corrosion resistance of the three carbon materials.

2. Experimental

2.1. Materials

$La_{0.5}Sr_{0.5}Mn_{0.5}Co_{0.5}O_{3-\delta}$ (LSMC) perovskite (10.2 $m^2\,g^{-1}$ BET surface area) was prepared and characterized with X-ray powder diffraction as described in our previous

work [26]. Vulcan XC-72R carbon and Shawinigan acetylene black were purchased from Cabot Corp. and Chevron Phillips Chem. Comp. respectively. Sibunit-152 carbon is a proprietary pyrolytic carbon of the Sibunit family [27] received from the Boreskov Institute of Catalysis, Novosibirsk (Russia) and obtained via deposition of pyrocarbon (through pyrolysis of gaseous hydrocarbons) on the surface of a technical carbon black followed by subsequent activation. All solutions were prepared using high-purity water (18.2 MΩ cm, <1 ppb TOC, Purelab).

2.2. Electrode preparation

Carbon materials were immobilized on a glassy carbon (GC) disk electrode mirror-like polished using alumina/water pastes with 1 and 0.3 μm alumina particle sizes. For the preparation of a 91 μg cm^{-2} carbon loading a certain portion of the carbon powder was mixed with a calculated amount of water to form 0.6 mg ml^{-1} suspension, which was then treated in the ultrasound bath for *ca*. 10 min. To obtain homogeneously distributed and reproducible electrode layers, three 10 μl portions of the ink were subsequently drop-cast onto the GC disk using a micropipette, with and intermediate drying step under a slow N_2 gas stream. At the final stage, 6 μl portion of an alkaline ionomer AS-4 (Tokuyama Company) aqueous solution was pipetted onto the deposited layer and dried under N_2, to provide the ionomer content of *ca*. 1.3 μg cm^{-2}. The electrochemical tests with a bare GC disk electrode were also performed in the presence of ionomer for the sake of comparison.

LSMC was mixed (1:1 on the weight basis) with carbon powders in the agate mortar. This mixture was used to prepare an aqueous suspension (0.1 mg ml^{-1}) and deposited on the GC disk electrode as described above to attain 15 μg cm^{-2} loadings for each of the components. Lower loadings for the LSMC/carbon compared to the bare carbon electrodes

were used for decreasing the OER currents and thus minimizing the effect of the oxygen bubble formation on the RRDE operation.

2.3. Electrochemical measurements

Electrochemical measurements were performed in a three-electrode Teflon cell with the upper part made of Pyrex glass. 1 M NaOH solution was prepared from the 50 wt.% NaOH aqueous solution (Alfa Aesar). The working electrode was an RRDE with a GC disk (5 mm diameter) and gold ring (7.5 mm outer diameter and 6.5 mm inner diameter) equipped with a MSR rotator system, both from Pine Research Inst. The counter electrode was a smooth Pt wire and the reference electrode was a Hg/HgO electrode filled with 1 M NaOH. All potentials reported below were recalculated into the scale of the reversible hydrogen electrode (RHE): $E_{\mathrm{RHE}} = E_{\mathrm{Hg/HgO/1\ M\ NaOH}} + 0.930$ V. Measurements were performed using an Autolab bipotentiostat-galvanostat PGSTAT302N equipped with a linear scan generator module. The temperature of the cell was kept at 25°C using a water-cooled thermostatic bath. The cell resistance was determined from a high-frequency intercept of electrochemical impedance hodographs recorded for each electrode layer at OER potentials in the 0.1 Hz to 100 kHz frequency range with an amplitude of 5 mV.

The RRDE collection efficiency N (24.5% at 1600 rpm) was determined from the ring and disk current ratios in 10 mM $K_3[Fe(CN)_6]$ + 1 M NaOH solution. This value is in fair agreement with the theoretical value (25%). The ring potential (+0.3 V vs. RHE) for the RRDE studies of the OER was chosen based on the oxygen reduction reaction (ORR) cyclic voltammograms (CVs) recorded on the Au ring in the O_2-saturated 1 M NaOH solution [26]. Before the RRDE measurements the gold surface of the ring electrode was polished using alumina/water pastes and cleaned by applying 20–50 potential cycles in the interval from 0.03 to 1.53 V at 200 mV s^{-1}. To determine the OER contribution to the overall anodic disk currents, faradaic oxygen efficiencies ε were calculated as $\varepsilon = (4/n_{\mathrm{ORR}})\, j_{\mathrm{Ring}} / (N\, j_{\mathrm{Disk}})$, where

($4/n_{ORR}$) is the ratio of the number of electrons transferred in the OER at the disk electrode and in the ORR at the ring electrode (n_{ORR} =2 for the gold ring, see Ref. [26]), j_{Ring} and j_{Disk} are the ring and disk currents respectively.

2.4. Materials characterization

N_2 physisorption isotherms were measured with TriStar Surface Area and Porosity Analyzer (Micromeritics, USA) and used to determine the specific surface area by multiple-point Brunauer–Emmett–Teller (BET) approach (S_{BET}). Surface area (S_{BJH}) of the pores with the size ranging from 1.7 nm to 300 nm was determined using the BJH method from the adsorption branch of the isotherm. The micropore area and volume were obtained by applying the *t*-plot method of Lippens and de Boer to the adsorption data. The corresponding values are given in Table 1.

Transmission electron microscopy (TEM) images of carbon materials, LSCM and LSCM/carbon compositions before and after anodic oxidation were made using JEOL 2100LaB6 microscope operated at 200 kV and equipped with an X-ray Energy Dispersive Spectrometer (EDX) for elemental analysis. After anodic oxidation GC disc supported carbon samples and LSCM/carbon compositions were washed with water and dried. For TEM measurements these samples as well as the samples before the anodic oxidation were dry-transferred onto carbon-coated copper grids. Substructural characteristics of the carbon materials (the sizes of the X-ray coherent scattering domains , L_a and L_c, and the interlayer spacing, d_{002}) were taken from our previous work [28].

Carbon samples studied in this work strongly differ in terms of their morphology and substructural characteristics. The surface area of acetylene black and Sibunit-152 is dominated by mesopores, while for Vulcan XC-72R, micro- and mesopores give comparable contributions to S_{BET} (Table 1). Considering the above, for Vulcan XC-72R the BJH surface (S_{BJH}), corresponding to the area of meso- and small macropores (pore size interval from

1.7 to 300 nm) is much inferior of S_{BET}, while for Sibunit-152 and for acetylene black, S_{BET} and S_{BJH} have comparable values. As one may see from TEM images of Fig. S1 in the Supplementary information, both acetylene black and Vulcan XC-72R consist of spherical so-called 'primary' particles (*ca*. 40 and *ca*. 20-30 nm diameter, correspondingly). However, packing of quasi-graphitic crystallites within these particles is quite different for these carbon materials. In acetylene black, graphene sheets are fairly well ordered and aligned parallel to the surface of primary particles (Fig. S1c). As a consequence, the surface of acetylene black is dominated by basal planes. This has been confirmed by Simonov [29] via adsorption of $PdCl_2$, the latter suggesting that the surface coverage of basal planes (θ_{basal}) is equal to *ca*. 0.76. High contribution of the basal plane to the surface is in agreement with the high contact angle (Table 1, Ref. [28]). For Vulcan XC-72R the surface termination is quite different as evidenced by TEM analysis (Fig. S1b), as well as by $PdCl_2$ adsorption [29], both suggesting comparable contribution of the basal and edge planes to the surface. Furthermore, graphene sheets in Vulcan XC-72R are significantly shorter, forming smaller quasi-graphitic crystallites. Sibunit-152 carbon has a very different morphology with a shell of pyrocarbon around carbon black particles (Fig. S1a). These carbon black particles are partially gasified during the activation procedure. The surface of Sibunit-152 is more or less equally represented by the basal and the edge planes (Table 1).

3. Results and discussion

3.1. Potential dependence of the OER and corrosion currents on carbon materials

Prior to corrosion measurements carbon materials were characterized in the pseudo-capacitive potential range from 0.93 to 1.03 V (where no faradaic processes are expected). CVs of the bare GC and GC-supported pristine carbon powders are shown in Fig. S1d, demonstrating an increase of pseudo-capacitance in the series: Acetylene black <

Sibunit-152 < Vulcan XC-72R. The capacitance values (C_{BET}) of carbon materials extracted from the CVs by integration (without subtraction of the GC contribution) and normalization to the BET surface area, are collected in Table 1. The C_{BET} values span from *ca*. 2 to *ca*. 7 μF $cm^{-2}{}_{BET}$, being in an overall agreement with the literature data reported for acetylene black (*ca*. 5 μF $cm^{-2}{}_{BET}$ in 0.5 M H_2SO_4 [30] and *ca*. 3.4 μF cm^{-2} in 4 M NaOH [13]), Vulcan XC-72(R) (*ca*. 8 μF $cm^{-2}{}_{BET}$ in 0.1 M H_2SO_4 [31], *ca*. 10 μF $cm^{-2}{}_{BET}$ in 0.5 M H_2SO_4 [30], *ca*. 5 μF $cm^{-2}{}_{BET}$ in 1 M H_2SO_4 [32], *ca*. 6 μF $cm^{-2}{}_{BET}$ in 6 M KOH [33] and *ca*. 10 μF $cm^{-2}{}_{BET}$ in 31% KOH [34]), and Sibunit carbon (*ca*. 13 μF $cm^{-2}{}_{BET}$ in 30% H_2SO_4 [35] for Sibunit carbons with S_{BET} from 330 to 480 $m^2\ g^{-1}$). Higher C_{BET} values reported by Ryabova et al. [28] for the same carbon materials may be explained by a wider potential interval applied by the authors of Ref. [28], resulting in a discharge of surface oxygen-containing functionalities.

To account for a limited accessibility of micropores, in Table 1 we also tabulated values of $C_{BJH,}$ which were obtained by normalizing the total capacitance to the BJH surface area. C_{BJH} values decrease from Vulcan XC-72R to Sibunit-152 and then acetylene black corroborating noticeable difference in the proportion of basal and edge planes exposed to the surface of these materials (Table 1 and Refs. [28,29]). While the exact values of capacitance for the basal C_{basal} and the edge C_{edge} plane of graphite vary in the literature, it is well established that C_{basal} is much inferior of C_{edge} [36]. For example, Randin and Yeager studied stress-annealed pyrolytic graphite in 1 M NaOH and reported *ca*. 3 and 90 μF cm^{-2} for C_{basal} and C_{edge}, correspondingly [37,38], while Rice and McCreery [39] communicated somewhat different values of 1.9 μF cm^{-2} and 70 μF cm^{-2} in 1 M KCl for C_{basal} and C_{edge}, correspondingly. Following Rice and McCreery, Ryabova et al. [28] estimated the proportion of the edge and basal planes on the surface of carbon materials from the values of pseudocapacitance. Even if an incomplete wetting of the carbon surface cannot be fully discarded, one should notice very good agreement of the proportion of basal planes estimated from C_{BJH} and from $PdCl_2$ adsorption values (Table 1).

To investigate the anodic behavior of carbon materials, we applied the RRDE method and measured current transients by applying consecutive (15 min long) potential steps from 1.53 V up to 2.03 V in 50-100 mV increments (Fig. 1). By measuring both disk (Fig. 1a) and ring (Fig 1b) currents it was possible to separate the OER from the carbon corrosion, and calculate the OER current efficiency ε (Fig. 1c). At potentials less than or equal to +1.53 V the OER efficiency is low, currents being dominated by the carbon corrosion. However, oxygen efficiencies (Fig. 1c) increase with the electrode potential and achieve 75–90% (depending on the type of carbon) in the potential interval from 1.68 to 1.73 V, then they somewhat decay, remaining fairly high (especially for acetylene black and Sibunit-152 carbon) even at 2.03 V. Similar behavior was reported for acetylene black in 30 wt.% KOH + 2 wt.% LiOH at 45°C [23]. Such a behavior is drastically different from that observed in acid, where the OER efficiency is negligible and anodic currents are dominated by carbon corrosion [22,40,41].

Since disk currents (Fig. 1a) comprise a sum of the OER and the carbon oxidation current, the latter can be calculated from the overall disk current as j_{Disk} (1 – ε). Fig. 2 represents carbon oxidation currents normalized either to the geometric electrode area (panel a), or to the residual carbon mass (panel b, see figure caption for details), or to the residual surface area (panel c, see figure caption for details). Normalization of the current to the BET area most likely leads to an underestimation of the corrosion current density, especially for the Vulcan XC-72R carbon, since the latter contains large fraction of micropores (Table 1) that may not be accessible to the electrolyte. Current densities obtained by normalization to the BJH surface area are given in Fig. S2. Corrosion currents plotted in Fig. 2 are somewhat higher as compared to those reported in literature. For example, for acetylene black the following corrosion currents were reported: 2 mA g^{-1} at *ca*. 1.43 V vs. RHE in 4 M KOH at 25°C [13] and 9 mA g^{-1} at *ca*. 1.58 V vs. RHE in 30 wt.% KOH + 2 wt.% LiOH at 45°C [23]. Since water molecules participate in the carbon corrosion

process [13], it is very likely that an increase of the water concentration results in an increase of the corrosion rates. This effect was found for corrosion of the acetylene black [13] and the Neo Spectra carbon black [42] in H_3PO_4 solutions. Currents taken at the end of each 15 min transient are plotted (on a logarithmic scale) against the electrode potential in Fig. 3a and Fig. 3b. Even if the shape of the plots may be influenced by the non-steady-state character of the currents and materials transformation in the prior potential steps, it is interesting to note different current-potential dependence for the materials under study. In what follows this behavior will be discussed in connection with the microstructure of these carbon materials.

To provide *in situ* information regarding interfacial properties of carbon materials after anodic polarization, CVs were measured in the narrow (0.93 – 1.03 V) potential window right after anodic polarization, in the middle (after 1.68 V) and at the end of the stepwise polarization procedure (after 2.03 V). The corresponding charges are presented in Fig. S3a demonstrating drastically different behavior for the studied carbon materials. GC and Vulcan XC-72R may be considered as the extreme cases of a non-porous (GC) and a highly porous material (Vulcan XC-72R), demonstrating an ascending and a descending voltammetric charge, respectively. An increase of the charge may be attributed to the increase of the roughness factor and an ensuing increase of the total surface area (due to the preferential oxidation of the less ordered fraction of the electrode) observed for GC in previous publications [24], an increase of the ratio of the edge to basal graphene planes, as well as to the formation of oxygen-containing functionalities on the carbon surface [13,24,43]. Indeed, formation of oxygen functionalities is usually believed to increase the pseudocapacitance. However, Zuleta et al. [44] when studying microporous carbon corrosion in 6 M KOH, reported that while oxidation at low potentials (up to *ca*. 1.2 V vs. RHE) results in a capacitance increase, oxidation at higher potentials (up to *ca*. 1.4 V vs. RHE) leads to a decrease of pseudocapacitance presumably due to the formation of surface

functionalities containing two oxygen atoms. A decrease of the charge observed for Vulcan XC-72R may be attributed to the pore blocking by the products of electrolysis (various products may result from the anodic polarization of carbon in alkaline media, including carbonates, CO [13,22,23], soluble organic residues [23,24], and/or oxygen bubbles [13]). Since Vulcan XC-72R contains a large fraction of micropores, it is interesting to note that Zuleta et al. [44] observed a systematic decrease of diffusion coefficients in small (*ca*. 0.7 nm diameter) micropores upon carbon oxidation, which they attributed to the pore constriction and/or blocking by the corrosion products. In addition, one cannot exclude detachment of carbon clusters from the electrode surface [45]. Sibunit-152 and acetylene black demonstrate an intermediate case with the charge increasing after polarization in the potential interval from +1.53 V to +1.68 V, and then decreasing significantly after polarization at higher potentials. It thus appears that the voltammetric charge evolves with time and potential in a complex non-monotonic manner, and that 'steady-state' can hardly be achieved on the time scale of a conventional laboratory experiment.

For this work, we have purposely chosen carbon materials, which differ significantly in terms of substructural parameters (L_a, L_c and d_{002}), proportion of the basal and edge planes to the surface, and S_{BET} (Table 1). It is widely accepted that both the electrochemical [13,14,16,46–48] and chemical [13,49–51] corrosion resistance of carbon materials depends on their microstructure, increasing with the extent of their crystalline order. For example, Yuzhanina et al. [41] investigated corrosion of compact carbon materials with different structures (pyrolytic graphite, glassy carbon, carbositall, graphite) in the pH interval from 0.9 till 14 and potentials from +1.4 to +2.2 V vs. RHE and reported higher corrosion resistance for ordered materials with fewer structural defects. According to morphological and substructural characteristics of the studied materials, their rate of corrosion was expected to increase in the sequence Acetylene black < Sibunit-152 < Vulcan XC-72R. However Figs. 2-3 confirm this trend only for potentials below +1.63 and above

+1.93 V vs. RHE, i.e. at potentials with the lowest oxygen faradaic efficiency (Fig. 1). In the intermediate potential range, acetylene black, which demonstrates the highest OER currents in the series, seems to be most prone to corrosion. In what follows TEM imaging will corroborate this finding. We assume that the oxygen evolution on carbon materials can accelerate carbon corrosion, probably due to the formation of some active OER intermediates [52], which chemically attack the surface of carbon materials. For example, OH-radicals may be formed through decomposition of H_2O_2 whose formation during the OER has been postulated [53], but, to the best of our knowledge, not confirmed yet. Formation of OH-radicals under positive polarization in alkaline media and their detrimental effect on the stability of carbon materials has been hypothesized in several publications [24,40,45]. Thus, carbon activity in the OER should be taken into account as an independent factor when analyzing corrosion resistance of carbon materials in alkaline media. In addition, one should take into account a structural evolution in the course of corrosion, which may smear correlation between the microstructure of pristine materials and their corrosion rate under harsh conditions and/or long times.

It is instructive to compare lifetimes of carbon materials (that is time required for their complete anodic dissolution) under polarization. In order to *roughly* estimate the apparent lifetime, we applied Faraday's law, and made several assumptions. First, we considered currents achieved at the end of each transient as steady-state. Second, we assumed $4e^-$ oxidation supposing that surface passivation currents were negligible at the end of each transient. Thus calculated lifetimes are plotted in Fig. 3c. They decrease with an increase of the anodic potential and are seemingly insufficient for any industrial application. Note however that short (15 min) current transients are hardly appropriate for a precise determination of the durability of carbon materials. In what follows we studied anodic behavior of carbon materials for a longer period of time (5 hours) aiming to attain steady-state conditions.

3.2. Time dependence of anodic currents on carbon materials

Time-dependent anodic behavior was investigated by applying potential of 1.63 V for 5 h and using RRDE for separating the OER and the carbon corrosion current. It should be noted however that formation of oxygen bubbles significantly affected the accuracy of the measurements, especially for acetylene black, the most active OER catalyst among carbon materials studied in this work (see below). Fig. 4 shows disc (panel a) and ring currents (panel b), and OER efficiencies (panel c) calculated as described above.

For the bare GC electrode both the disk and the absolute value of the ring current increase, the OER efficiency approaching 100% after *ca*. 3 h of electrolysis. Such a behavior supports the above assumption regarding preferential corrosion of the least ordered fraction of carbon, leaving behind more corrosion resistant fragments. Ascending transients were also observed for acetylene black. However, for acetylene black after 3 h of polarization at 1.63 V the current at the ring attained a reproducible plateau, which resulted in a decrease of the calculated oxygen efficiency. The occurrence of the plateau and the noise observed at the ring may be attributed to the formation of oxygen bubbles (due to a high rate of the oxygen evolution) that block the surface of the disc, and hinder transfer of dissolved oxygen from the disk to the ring electrode [26,54–56]. Indeed, when the RRDE tip was pulled out from the cell after 5 h of the anodic polarization, and oxygen bubbles were removed, the oxygen efficiency measured during subsequent 10 min of polarization at the same potential (see inset in Fig. 4c), amounted to *ca*. 95%. It should be kept in mind that an underestimation of the oxygen efficiency unavoidably leads to an overestimation of the corrosion current (see discussion below).

Very different behavior is observed for Vulcan XC-72R carbon showing a descending transient similar to what has been observed during carbon corrosion in acid electrolytes [13,14,16]. The OER efficiency for Vulcan XC-72R varies between 60 and 80%. For Sibunit-

152 both disc and ring currents pass through a maximum. Similar non-monotonous behavior was reported for multiwall carbon nanotubes at +1.8 V vs. RHE in 0.5 M H_2SO_4 [17] and attributed to the preferential oxidation of amorphous carbon and less ordered carbon fragments at the beginning of the transient. We believe that this conclusion applies to Sibunit-152 as well, which in what follows will be corroborated using TEM.

Cyclic voltammetry was utilized to provide information regarding interfacial properties of carbon materials after anodic polarization. First, CVs were recorded in a narrow potential interval of 0.93 to 1.03 V (not shown), and then in a wider potential interval of 0.05 to 1.03 V (Fig. S4). Charges calculated from CVs acquired in the narrow potential interval are plotted in Fig. S3b and reflect phenomena already discussed in section 3.1. For GC the observed increase of the charge is most likely related to the surface roughening and formation of the surface oxygen functionalities [24]. TEM investigation presented below supports surface roughening also for acetylene black. For Vulcan XC-72R, the charge obtained by integration of CVs acquired in a narrow potential interval [0.93 – 1.03 V] right at the end of the 5 h transient was *ca*. 3 times inferior of the initial charge (Fig. S3b). In the meantime, steady-state CVs acquired in a wide potential interval [0.05 – 1.03 V] demonstrate an increase of pseudocapacitance for all carbon materials, which may be attributed to the formation of surface functional groups, and possibly also to the surface roughening and hydrophilization, both resulting in an increase of the accessible surface area. We thus conclude that for Vulcan XC-72R (and likely also for Sibunit-152) oxygen bubbles and corrosion products block significant fraction of the pores, leading to the decrease of the current in time. For acetylene black such pore blocking occurs to a lesser extent due to the smaller pore volume and lower tortuosity of the pores. Once voltammograms are extended down to 0.05 V, oxygen accumulated in the pores is reduced resulting in an increase of the accessible surface area, which translates in higher pseudocapacitive currents in Fig. S4.

Carbon oxidation currents calculated from the corresponding RRDE transients are shown in Fig. 5, normalized to the geometric electrode surface area (panel a), residual carbon mass (panel b) and surface area of carbon materials, the latter calculated from the initial BET surface area and the residual carbon mass (panel c). Only Sibunit-152 and Vulcan XC-72R carbon materials demonstrate virtually steady-state values of corrosion currents after 4-5 hours of the anodic polarization. The corrosion current calculated for acetylene black is significantly overestimated due to the oxygen efficiency underestimation (see above). Using *ca*. 95% oxygen efficiency achieved after the removal of oxygen bubbles (inset in Fig. 4c), we recalculated the oxidation current of acetylene black (the dashed curve in Fig. 5). Taking into account the error in the oxygen efficiency calculation (±4%), carbon corrosion currents at 1.63 V and *after* 5 h of polarization are estimated as 0.76 ± 0.08 A g^{-1} or 0.92 ± 0.12 μA cm^{-2}_{BET} for Sibunit-152, 0.10 ± 0.02 A g^{-1} or 0.05 ± 0.01 μA cm^{-2}_{BET} for Vulcan XC-72R and 1.1 ± 0.9 A g^{-1} or 1.7 ± 1.4 μA cm^{-2}_{BET} for acetylene black. The estimates of these currents normalized to initial BET areas suffer from the uncertainty of specific surface area evolution in the course of corrosion.

Lifetimes of carbon materials estimated from the current values achieved at the end of 5 h transients amount to 90 ± 20, 12 ± 2 and 8 ± 6 h for Vulcan XC-72R, Sibunit-152 and acetylene black, respectively, instead of *ca.* 20–30 h estimated at short times (Fig. 3). Note that these values can be underestimated because of the oxygen bubble generation and possible GC contribution to the measured currents.

By integrating corrosion currents shown in Fig. 5, the mass loss of carbon materials after 5 h of polarization can be estimated using Faraday's law. The corresponding values amount to *ca*. 16% for Vulcan XC-72R, *ca*. 28% for Acetylene black and *ca*. 43% for Sibunit-152.

TEM was employed to check morphological changes induced by carbon corrosion after 5 h of the anodic polarization at +1.63 V. For Vulcan XC-72R, the morphology was

largely preserved (Fig. S5). Some images of Vulcan XC-72R after polarization showed holes in the center of primary carbon globules. However, it is difficult to unambiguously attribute these holes to corrosion since TEM images of the pristine Vulcan XC-72R sample also showed some disordered domains and/or holes in the particle centers. For Sibunit-152 we did not observe any change in the structure of pyrolytic carbon (Fig. S6). Meanwhile, TEM images at lower magnification clearly showed formation of holes inside carbon globules (Fig. S7). Such morphology is typical for carbon materials of the Sibunit family obtained after prolonged steam activation [27,57] and suggests that during the anodic polarization the least ordered fraction of the sample, namely carbon black particles, degrades, leaving behind more ordered shells consisting of pyrolytic carbon. This conclusion agrees with the shape of the current transients (which pass through a maximum and then decay) and with the literature data for some other carbon materials (e.g. multiwall carbon nanotubes [17]). This observation suggests that carbon materials of the Sibunit family obtained after prolonged steam activation, resulting in total removal of carbon black particles, onto which pyrolytic carbon was deposited, may be less prone to electrochemical corrosion.

Significant morphological changes were observed for acetylene black after the anodic polarization. Indeed, at the surface of carbon globules one may see disordered fragments, and ragged graphene layers (Fig. 6). For pristine acetylene black particles, in agreement with the XRD data of Table 1, the interplanar (002) spacing estimated from the HRTEM density profiles (not shown) was similar to 0.35 nm, but increased up to 0.44 or sometimes even 0.50 nm in corroded zones. Note that authors of Ref. [58] could not visualize any signs of corrosion despite significant (more than 50%) mass loss after the exposure of acetylene black to *ca*. 1.57 V vs. RHE in 30 wt.% KOH at 55°C during 20 days. They supposed that corrosion of acetylene black occurs in amorphous regions surrounding graphene ribbons, the latter being less prone to corrosion. Note that Yi et al. [17] applied high resolution TEM to study anodic degradation of multiwall carbon nanotubes at +1.8 V

vs. RHE in 0.5 M H_2SO_4 for 10 h and observed destruction of the nanotube sidewalls and collapse of graphitic layers resembling that observed in Fig. 6 of this work.

TEM data shown in this work are in agreement with the RRDE data and confirm that the rate of carbon corrosion increases in the sequence Vulcan XC-72R < Sibunit-152 < Acetylene black. One can note that the OER activity of bare carbon materials also increases in this sequence. The influence of the OER on the carbon corrosion may be illustrated by considering a double logarithmic plot of corrosion currents *vs*. time (Fig. S8). At short times currents decay following a $i = kt^{-n}$ law documented by Kinoshita [42], scaling with the extent of structural order Vulcan XC-72R > Sibunit-152 > Acetylene black. However, an increase of the oxygen evolution rate (Fig. 4) breaks this trend. Therefore, Vulcan XC-72R with the least ordered structure and the lowest OER-activity demonstrates a small mass loss and does not show noticeable destruction of primary particles (Fig. S5). Its corrosion current continuously decays (following $i \approx kt^{-0.5}$ dependence) similar to what has been observed in acid electrolytes [13,16]. This may be attributed to the surface passivation followed by slow corrosion propagation via micropores (*cf*. high fraction of micropores in Vulcan XC-72R) towards the centers of primary particles. Sibunit-152 and Acetylene black, despite their higher degree of structural order, demonstrate higher mass loss (Fig. S7) and noticeable morphology changes (Fig. S7 and Fig. 6). We attribute this to the higher OER activities of these carbon materials. Especially remarkable is the observed degradation of the basal planes of acetylene black (Fig. 6), which may be tentatively attributed to their higher OER activity and formation of corrosive OER (e.g. radical) intermediates. Another phenomenon, which might affect the rate of corrosion, is intercalation accompanying carbon oxidation [59]. Indeed, it has been documented that in highly imperfect carbon materials (like Vulcan XC-72R in this work) the intercalation occurs less readily as a consequence of high extent of cross-linking of graphene layers [60].

3.3. Influence of LSMC on carbon corrosion

In order to explore influence of an oxide OER catalyst on the carbon corrosion, $La_{0.5}Sr_{0.5}Mn_{0.5}Co_{0.5}O_{3-\delta}$ perovskite oxide was mixed with either of the three carbon materials, now operating as conductive additives, and polarized at +1.63 V for 5 h. If carbon corrosion was strongly accelerated in the presence of LSMC, one would expect a decay of the OER activity approaching that of the bare oxide.

RRDE transients of LSMC/carbon compositions, bare oxide and bare GC are shown in Fig. 7. Simultaneously recorded disk (panel a) and ring (panel b) currents confirm the occurrence of the OER. For the bare oxide the OER currents increase with time, which can be attributed to the GC substrate contribution, since a low catalyst loading (15 μg cm^{-2}_{geo}) was used to minimize the oxygen bubble formation. Similar minima in the faradaic efficiency plots (panel c) for the GC-supported oxide and for bare GC are also in favor of the GC contribution. The disk currents for the oxide/carbon compositions are much higher than the current for the bare oxide and remain such after 5h of polarization, suggesting that a significant fraction of the carbon additives must be preserved.

Unfortunately, oxygen bubble formation (for LSMC/Vulcan XC-72R and LSMC/Sibunit-152 noticeable at long measurement times, and for the most active LSMC/ Acetylene black observed already at short times) decreases the collection efficiency resulting in an erroneous measurement of the OER efficiency (Fig. 7c). To estimate faradaic efficiencies at the end of the transient, oxygen bubbles were manually removed as described above, and anodic polarization was applied for another 10 min (Fig. S9). After the bubbles removal oxygen efficiencies achieved values from 93±4 to 96±4% (Fig. S9c). Small contribution of the carbon corrosion to the total currents hinders accurate determination of the former.

One may see that the OER activity of LSMC/carbon compositions (Fig. 7) correlates with the OER activity of bare carbon materials (Fig. 4), increasing in the sequence Vulcan

XC-72R < Sibunit-152 < Acetylene black. This may be explained by synergy between the two components, whose nature is not fully understood yet.

One may notice that the OER currents of the oxide/carbon compositions increase with time for all studied materials. In order to exclude transformation of the LSMC catalyst, which might be at the origin of the time-dependent OER activity, TEM measurements were performed after 5 h of the anodic polarization for two representative carbon materials: acetylene black and Vulcan XC-72R. Careful analysis of numerous images did not show any sign of either oxide or carbon degradation. Indeed, TEM images of Fig. S10 demonstrate oxide particles, which after 5h polarization do not show formation of a disordered surface layer. Moreover, EDX maps of oxide particles after 5 h of anodic polarization (Fig. 8) did not show formation of a surface layer depleted in either of the constituents, as compared with pristine oxide particles (Fig. S11). Figs. 6d and S5c demonstrate acetylene black and Vulcan XC-72R particles after polarization, which do not show either any sign of degradation or presence of any transition metal containing species redeposited on the carbon surface. This is particularly surprising for acetylene black, whose morphology was strongly altered by corrosion in the absence of the LSMC oxide. The experimental observation suggests that carbon corrosion is attenuated in the presence of the LSMC OER catalyst. Note that previous publications reported an improved carbon durability under *constant current operation*, and explained it by the decrease of the OER overpotential in the presence of oxide [61,62]. In this work attenuation of carbon corrosion is observed under *potentiostatic conditions* and may be tentatively attributed to the role of LSMC oxide as a scavenger of active (e.g. radical) OER intermediates.

4. Conclusions

We investigated the anodic behavior of some carbon materials (Sibunit-152, Vulcan XC-72R and Acetylene black) to explore their promise as conductive additives for

insufficiently conductive transition metal oxide OER catalysts operating in alkaline media. We applied the RRDE technique to separate carbon corrosion from the OER currents and studied simultaneously occurring oxygen evolution and carbon corrosion. We found that for bare carbon materials a decrease of the rate of corrosion with the extent of structural order is only observed at short times and moderate OER overpotentials. Our study reveals that carbon materials with a higher intrinsic OER activity show lower durability and tentatively attributed this to the formation of active (e.g. radical) OER intermediates, provoking chemical degradation of carbon materials. We then studied composite OER catalysts consisting of a $La_{0.5}Sr_{0.5}Mn_{0.5}Co_{0.5}O_{3-\delta}$ perovskite oxide mixed with carbon and discovered that the oxide component protects the carbon counterpart from corrosion. This finding gives hope that carbon materials, being thermodynamically unstable in the potential interval of the OER, may nevertheless survive harsh conditions, to which an anode of a water electrolysis cell is exposed. In this regard, it might be interesting to explore influence of various types of OER catalysts on carbon corrosion. Moreover, long-term durability studies under industrially relevant electrolysis conditions (in particular at higher temperatures and in the presence of polymer rather than liquid electrolytes) are required to better evaluate promise of carbon materials for electrolysis applications. On the other hand, search for electronically conductive carbon-free OER catalysts remains the most relevant OER topic.

Acknowledgements

The authors are indebted to Tokuyama Company (Japan) for supplying AS-4 alkaline ionomer. Denis M. Antipin, Alexander Ye. Baranchikov and Anna S. Ryabova are gratefully acknowledged for the synthesis of the $La_{0.5}Sr_{0.5}Mn_{0.5}Co_{0.5}O_{3-\delta}$ perovskite, its BET characterization and TEM characterization of some carbon materials, respectively. Financial support from the National Centre for Scientific Research (France) and Russian

Foundation for Basic Research (Russia) within a joint ERA.NET.RUS project (NANO-MORF, CNRS ID 270, RFBR, Russia ID 16-53-76014) is gratefully appreciated. French Embassy in Russia for Vernadsky PhD scholarship to I.F. is specially acknowledged.

Appendix A. Supplementary data

Supplementary data related to this article can be found at https://doi.org/

References

[1] P. Trogadas, T.F. Fuller, P. Strasser, Carbon as catalyst and support for electrochemical energy conversion, Carbon N. Y. 75 (2014) 5–42. doi:https://doi.org/10.1016/j.carbon.2014.04.005.

[2] N.-T. Suen, S.-F. Hung, Q. Quan, N. Zhang, Y.-J. Xu, H.M. Chen, Electrocatalysis for the oxygen evolution reaction: recent development and future perspectives, Chem. Soc. Rev. 46 (2017) 337–365. doi:10.1039/C6CS00328A.

[3] R. Mohamed, X. Cheng, E. Fabbri, P. Levecque, R. Kötz, O. Conrad, T.J. Schmidt, Electrocatalysis of Perovskites: The Influence of Carbon on the Oxygen Evolution Activity, J. Electrochem. Soc. 162 (2015) F579–F586. doi:10.1149/2.0861506jes.

[4] W.G. Hardin, J.T. Mefford, D.A. Slanac, B.B. Patel, X. Wang, S. Dai, X. Zhao, R.S. Ruoff, K.P. Johnston, K.J. Stevenson, Tuning the Electrocatalytic Activity of Perovskites through Active Site Variation and Support Interactions, Chem. Mater. 26 (2014) 3368–3376. doi:10.1021/cm403785q.

[5] L. Han, S. Dong, E. Wang, Transition-Metal (Co, Ni, and Fe)-Based Electrocatalysts for the Water Oxidation Reaction, Adv. Mater. 28 (2016) 9266–9291. doi:10.1002/adma.201602270.

[6] J.S. Kim, B. Kim, H. Kim, K. Kang, Recent Progress on Multimetal Oxide Catalysts for the Oxygen Evolution Reaction, Adv. Energy Mater. 8 (2018) 1702774. doi:10.1002/aenm.201702774.

[7] M.-I. Jamesh, X. Sun, Recent progress on earth abundant electrocatalysts for oxygen evolution reaction (OER) in alkaline medium to achieve efficient water splitting – A review, J. Power Sources. 400 (2018) 31–68. doi:10.1016/j.jpowsour.2018.07.125.

[8] M. Chen, L. Wang, H. Yang, S. Zhao, H. Xu, G. Wu, Nanocarbon/oxide composite catalysts for bifunctional oxygen reduction and evolution in reversible alkaline fuel cells: A mini review, J. Power Sources. 375 (2018) 277–290. doi:https://doi.org/10.1016/j.jpowsour.2017.08.062.

[9] V.F. Mattick, X. Jin, R.E. White, K. Huang, Understanding the role of carbon in alkaline oxygen electrocatalysis: A case study on $La_{0.6}Sr_{0.4}CoO_{3-\delta}$/Vulcan carbon composite electrocatalyst, Int. J. Hydrogen Energy. 44 (2019) 2760–2769. doi:https://doi.org/10.1016/j.ijhydene.2018.12.048.

[10] J. Zhang, Z. Zhao, Z. Xia, L. Dai, A metal-free bifunctional electrocatalyst for oxygen reduction and oxygen evolution reactions, Nat. Nanotechnol. 10 (2015) 444. doi:10.1038/nnano.2015.48.

[11] Y.-T. Pi, X.-Y. Xing, L.-M. Lu, Z.-B. He, T.-Z. Ren, Hierarchical porous activated carbon in OER with high efficiency, RSC Adv. 6 (2016) 102422–102427. doi:10.1039/C6RA19333A.

[12] X. Lu, W.-L. Yim, B.H.R. Suryanto, C. Zhao, Electrocatalytic Oxygen Evolution at Surface-Oxidized Multiwall Carbon Nanotubes, J. Am. Chem. Soc. 137 (2015) 2901–2907. doi:10.1021/ja509879r.

[13] K. Kinoshita, Carbon: Electrochemical and Physicochemical Properties, John Wiley and Sons, New York, Chichester, Brisbane, Toronto, Singapore, 1988, pp. 195-197, 293-387.

[14] K. Artyushkova, S. Pylypenko, M. Dowlapalli, P. Atanassov, Structure-to-property relationships in fuel cell catalyst supports: Correlation of surface chemistry and morphology with oxidation resistance of carbon blacks, J. Power Sources. 214 (2012) 303–313. doi:https://doi.org/10.1016/j.jpowsour.2012.04.095.

[15] S.C. Ball, S.L. Hudson, D. Thompsett, B. Theobald, An investigation into factors affecting the stability of carbons and carbon supported platinum and platinum/cobalt alloy catalysts during 1.2V potentiostatic hold regimes at a range of temperatures, J. Power Sources. 171 (2007) 18–25. doi:https://doi.org/10.1016/j.jpowsour.2006.11.004.

[16] O. V Cherstiouk, A.N. Simonov, N.S. Moseva, S. V Cherepanova, P.A. Simonov, V.I. Zaikovskii, E.R. Savinova, Microstructure effects on the electrochemical corrosion of carbon materials and carbon-supported Pt catalysts, Electrochim. Acta. 55 (2010) 8453–8460. doi:https://doi.org/10.1016/j.electacta.2010.07.047.

[17] Y. Yi, J. Tornow, E. Willinger, M.G. Willinger, C. Ranjan, R. Schlögl, Electrochemical Degradation of Multiwall Carbon Nanotubes at High Anodic Potential for Oxygen Evolution in Acidic Media, ChemElectroChem. 2 (2015) 1929–1937. doi:10.1002/celc.201500268.

[18] L. Castanheira, W.O. Silva, F.H.B. Lima, A. Crisci, L. Dubau, F. Maillard, Carbon Corrosion in Proton-Exchange Membrane Fuel Cells: Effect of the Carbon Structure, the Degradation Protocol, and the Gas Atmosphere, ACS Catal. 5 (2015) 2184–2194. doi:10.1021/cs501973j.

[19] Z.Y. Liu, B.K. Brady, R.N. Carter, B. Litteer, M. Budinski, J.K. Hyun, D.A. Muller, Characterization of Carbon Corrosion-Induced Structural Damage of PEM Fuel Cell Cathode Electrodes Caused by Local Fuel Starvation, J. Electrochem. Soc. 155 (2008) B979–B984. doi:10.1149/1.2956198.

[20] Z.Y. Liu, J.L. Zhang, P.T. Yu, J.X. Zhang, R. Makharia, K.L. More, E.A. Stach,

Transmission Electron Microscopy Observation of Corrosion Behaviors of Platinized Carbon Blacks under Thermal and Electrochemical Conditions, J. Electrochem. Soc. 157 (2010) B906–B913. doi:10.1149/1.3391737.

[21] H. Schulenburg, B. Schwanitz, N. Linse, G.G. Scherer, A. Wokaun, J. Krbanjevic, R. Grothausmann, I. Manke, 3D Imaging of Catalyst Support Corrosion in Polymer Electrolyte Fuel Cells, J. Phys. Chem. C. 115 (2011) 14236–14243. doi:10.1021/jp203016u.

[22] G.N. Kokhanov, N.G. Milova, Effect of pH on the anodic oxidation process of graphite, Elektrochimiya. 5 (1969) 93–96.

[23] P.N. Ross, H. Sokol, The Corrosion of Carbon Black Anodes in Alkaline Electrolyte: I. Acetylene Black and the Effect of Cobalt Catalyzation, J. Electrochem. Soc. 131 (1984) 1742–1750. doi:10.1149/1.2115953.

[24] Y. Yi, G. Weinberg, M. Prenzel, M. Greiner, S. Heumann, S. Becker, R. Schlögl, Electrochemical corrosion of a glassy carbon electrode, Catal. Today. 295 (2017) 32–40. doi:https://doi.org/10.1016/j.cattod.2017.07.013.

[25] I.S. Filimonenkov, G.A. Tsirlina, E.R. Savinova, Conductive additives for oxide-based OER catalysts: A comparative RRDE study of carbon and silver in alkaline medium, Electrochim. Acta. 319 (2019) 227–236. doi:https://doi.org/10.1016/j.electacta.2019.06.154.

[26] I.S. Filimonenkov, S.Y. Istomin, E. V Antipov, G.A. Tsirlina, E.R. Savinova, Rotating ring-disk electrode as a quantitative tool for the investigation of the oxygen evolution reaction, Electrochim. Acta. 286 (2018) 304–312. doi:https://doi.org/10.1016/j.electacta.2018.08.056.

[27] Y.I. Yermakov, V.F. Surovikin, G. V Plaksin, V.A. Semikolenov, V.A. Likholobov, L. V Chuvilin, S. V Bogdanov, New carbon material as support for catalysts, React. Kinet. Catal. Lett. 33 (1987) 435–440. doi:10.1007/BF02128102.

[28] A.S. Ryabova, A. Bonnefont, P.A. Simonov, T. Dintzer, C. Ulhaq-Bouillet, Y.G. Bogdanova, G.A. Tsirlina, E.R. Savinova, Further insights into the role of carbon in manganese oxide/carbon composites in the oxygen reduction reaction in alkaline media, Electrochim. Acta. 246 (2017) 643–653. doi:https://doi.org/10.1016/j.electacta.2017.06.017.

[29] P. Simonov, H_2PdCl_4 adsorption as a chemical method for probing heterogeneity of carbon surfaces, from: P.A. Simonov, New Approaches for Studying Heterogeneity of Carbon Surfaces, CarboCat IV: The 4th Internat. Symp. on Carbon for Catal., November 7-10, 2010, Dalian, China, Abstracts, p.24 (plenary lecture). doi:10.13140/RG.2.2.27662.61763.

[30] V.A. Bogdanovskaya, L.A. Beketaeva, K. V Rybalka, B.N. Efremov, N.M. Zagudaeva, M. Sakashita, T. Iidzima, Z.R. Ismagilov, Nanosize catalysts based on carbon materials promoted by cobalt tetra(para-methoxyphenyl) porphyrin pyropolymer for oxygen electroreduction, Russ. J. Electrochem. 44 (2008) 293–302. doi:10.1134/S1023193508030063.

[31] M.D. Obradović, G.D. Vuković, S.I. Stevanović, V. V Panić, P.S. Uskoković, A. Kowal, S.L. Gojković, A comparative study of the electrochemical properties of carbon nanotubes and carbon black, J. Electroanal. Chem. 634 (2009) 22–30. doi:https://doi.org/10.1016/j.jelechem.2009.07.001.

[32] R.D.L. Smith, P.G. Pickup, Voltammetric quantification of the spontaneous chemical modification of carbon black by diazonium coupling, Electrochim. Acta. 54 (2009) 2305–2311. doi:https://doi.org/10.1016/j.electacta.2008.10.047.

[33] Y. Tang, Y. Liu, S. Yu, F. Gao, Y. Zhao, Comparative study on three commercial carbons for supercapacitor applications, Russ. J. Electrochem. 51 (2015) 77–85. doi:10.1134/S1023193514100127.

[34] E.G. Gagnon, The Triangular Voltage Sweep Method for Determining Double-Layer

Capacity of Porous Electrodes: IV . Porous Carbon in Potassium Hydroxide, J. Electrochem. Soc. 122 (1975) 521–525. doi:10.1149/1.2134250.

[35] A.S. Solyanikova, M.Y. Chayka, A. V Boryak, T.A. Kravchenko, A. V Glotov, I. V Ponomarenko, S.D. Kirik, Composite electrodes of electrochemical capacitors based on carbon materials with different structure, Russ. J. Electrochem. 50 (2014) 419–428. doi:10.1134/S1023193514050097.

[36] R.L. McCreery, Advanced Carbon Electrode Materials for Molecular Electrochemistry, Chem. Rev. 108 (2008) 2646–2687. doi:10.1021/cr068076m.

[37] J.-P. Randin, E. Yeager, Differential capacitance study on the basal plane of stress-annealed pyrolytic graphite, J. Electroanal. Chem. Interfacial Electrochem. 36 (1972) 257–276. doi:https://doi.org/10.1016/S0022-0728(72)80249-3.

[38] J.-P. Randin, E. Yeager, Differential capacitance study on the edge orientation of pyrolytic graphite and glassy carbon electrodes, J. Electroanal. Chem. Interfacial Electrochem. 58 (1975) 313–322. doi:https://doi.org/10.1016/S0022-0728(75)80089-1.

[39] R.J. Rice, R.L. McCreery, Quantitative relationship between electron transfer rate and surface microstructure of laser-modified graphite electrodes, Anal. Chem. 61 (1989) 1637–1641. doi:10.1021/ac00190a010.

[40] N.D. Vyet, D. V Kokoulina, L.I. Krishtalik, Investigation of electrochemical oxidation of a graphite anode. III. Composition of anodic products as affected by the state of anode surface and its polarization characteristics, Elektrochimiya. 8 (1972) 384–387.

[41] A. V Yuzhanina, D. V Kokoulina, L.A. Mashkovich, L.A. Dronseiko, A.F. Kuteinikov, Investigation of the electrochemical oxidation of carbon materials, Elektrochimiya. 15 (1979) 308–314.

[42] K. Kinoshita, J. Bett, Electrochemical oxidation of carbon black in concentrated phosphoric acid at 135°C, Carbon N. Y. 11 (1973) 237–247.

doi:https://doi.org/10.1016/0008-6223(73)90026-2.

[43] I.S. Filimonenkov, S.A. Urvanov, E.A. Zhukova, A.R. Karaeva, E.A. Skryleva, V.Z. Mordkovich, G.A. Tsirlina, Carbon nanotube cloth for electrochemical charge storage in aqueous media, J. Electroanal. Chem. 827 (2018) 58–63. doi:https://doi.org/10.1016/j.jelechem.2018.09.004.

[44] M. Zuleta, P. Björnbom, A. Lundblad, Effects of Pore Surface Oxidation on Electrochemical and Mass-Transport Properties of Nanoporous Carbon, J. Electrochem. Soc. 152 (2005) A270–A276. doi:10.1149/1.1843772.

[45] T. Wu, M. Han, X. Zhu, G. Wang, H. Zhang, H. Zhao, The electrochemical corrosion of an air thermally-treated carbon fiber cloth electrocatalyst with outstanding oxygen evolution activity under alkaline conditions, Chem. Commun. 55 (2019) 2344–2347. doi:10.1039/C9CC00398C.

[46] S. Pérez-Rodríguez, D. Sebastián, M.J. Lázaro, E. Pastor, Stability and catalytic properties of nanostructured carbons in electrochemical environments, J. Catal. 355 (2017) 156–166. doi:https://doi.org/10.1016/j.jcat.2017.09.019.

[47] C. Alegre, D. Sebastián, M.J. Lázaro, Carbon xerogels electrochemical oxidation and correlation with their physico-chemical properties, Carbon N. Y. 144 (2019) 382–394. doi:https://doi.org/10.1016/j.carbon.2018.12.065.

[48] S. Pérez-Rodríguez, D. Sebastián, M.J. Lázaro, Electrochemical oxidation of ordered mesoporous carbons and the influence of graphitization, Electrochim. Acta. 303 (2019) 167–175. doi:https://doi.org/10.1016/j.electacta.2019.02.065.

[49] V.A. Semikolenov, G.S. Litvak, G. V Plaksin, Effect of microstructure on the oxidation resistance of porous carbon materials in air, Inorg. Mater. 36 (2000) 591–594. doi:10.1007/BF02757960.

[50] R.L. Vander Wal, A.J. Tomasek, Soot oxidation: dependence upon initial nanostructure, Combust. Flame. 134 (2003) 1–9.

doi:https://doi.org/10.1016/S0010-2180(03)00084-1.

[51] C.K. Gaddam, R.L. Vander Wal, X. Chen, A. Yezerets, K. Kamasamudram, Reconciliation of carbon oxidation rates and activation energies based on changing nanostructure, Carbon N. Y. 98 (2016) 545–556. doi:https://doi.org/10.1016/j.carbon.2015.11.035.

[52] Y. Lin, Q. Lu, F. Song, L. Yu, A.K. Mechler, R. Schlögl, S. Heumann, Oxygen Evolution Reaction at Carbon Edge Sites: Investigation of Activity Evolution and Structure–Function Relationships with Polycyclic Aromatic Hydrocarbons, Angew. Chemie Int. Ed. 58 (2019) 8917–8921. doi:10.1002/anie.201902884.

[53] V.F. Mattick, X. Jin, T. Yang, R.E. White, K. Huang, Unraveling Oxygen Electrocatalysis Mechanisms on a Thin-Film Oxygen-Deficient Perovskite $La_{0.6}Sr_{0.4}CoO_{3-\delta}$, ACS Appl. Energy Mater. 1 (2018) 3937–3946. doi:10.1021/acsaem.8b00669.

[54] S. Dresp, F. Luo, R. Schmack, S. Kühl, M. Gliech, P. Strasser, An efficient bifunctional two-component catalyst for oxygen reduction and oxygen evolution in reversible fuel cells, electrolyzers and rechargeable air electrodes, Energy Environ. Sci. 9 (2016) 2020–2024. doi:10.1039/C6EE01046F.

[55] A.T. Swesi, J. Masud, M. Nath, Nickel selenide as a high-efficiency catalyst for oxygen evolution reaction, Energy Environ. Sci. 9 (2016) 1771–1782. doi:10.1039/C5EE02463C.

[56] Y. Qiu, L. Xin, W. Li, Electrocatalytic Oxygen Evolution over Supported Small Amorphous Ni–Fe Nanoparticles in Alkaline Electrolyte, Langmuir. 30 (2014) 7893–7901. doi:10.1021/la501246e.

[57] V.A. Semikolenov, Designing finely dispersed palladium catalysts on carbon supports, Russ. J. Appl. Chem. 70 (1997) 748–758.

[58] P.N. Ross, M. Sattler, The Corrosion of Carbon Black Anodes in Alkaline Electrolyte: III . The Effect of Graphitization on the Corrosion Resistance of Furnace Blacks, J.

Electrochem. Soc. 135 (1988) 1464–1470. doi:10.1149/1.2096029.

[59] S. Zhang, L. Zhu, H. Song, X. Chen, B. Wu, J. Zhou, F. Wang, How graphene is exfoliated from graphitic materials: synergistic effect of oxidation and intercalation processes in open, semi-closed, and closed carbon systems, J. Mater. Chem. 22 (2012) 22150–22154. doi:10.1039/C2JM35139K.

[60] N. Bartlett, B.W. McQuillan, Graphite Chemistry, in: M.S. Whittingham, A.J. Jacobson (Eds.), Intercalation Chem., Academic Press, New York, London, Paris, San Diego, San Francisco, São Paulo, Sydney, Tokyo, Toronto, 1982, pp. 19–53. doi:10.1016/B978-0-12-747380-2.50007-9.

[61] J. Yang, S. Park, K. young Choi, H.-S. Park, Y.-G. Cho, H. Ko, H.-K. Song, Activity-Durability Coincidence of Oxygen Evolution Reaction in the Presence of Carbon Corrosion: Case Study of $MnCo_2O_4$ Spinel with Carbon Black, ACS Sustain. Chem. Eng. 6 (2018) 9566–9571. doi:10.1021/acssuschemeng.8b01879.

[62] C.T. Alexander, A.M. Abakumov, R.P. Forslund, K.P. Johnston, K.J. Stevenson, Role of the Carbon Support on the Oxygen Reduction and Evolution Activities in $LaNiO_3$ Composite Electrodes in Alkaline Solution, ACS Appl. Energy Mater. 1 (2018) 1549–1558. doi:10.1021/acsaem.7b00339.

Table Captions

Table 1

Morphological, structural and electrochemical characteristics of carbon materials investigated in this work.

Figure Captions

Figure 1. RRDE transients of GC-supported carbon materials and bare GC at 1600 rpm in N_2-saturated 1 M NaOH with loadings of 91 μg cm^{-2}_{geo} following 15 min long potential steps from 0.93 V to higher anodic potentials (in the interval from 1.53 to 2.03 V as indicated in the figure): (a) disk currents; (b) normalized ring currents at E_{Ring} = 0.3 V; (c) oxygen faradaic efficiency. A short polarization step at 0.93 V was applied before (10 min) and after (5 min) each anodic potential step. Ring currents are corrected to the background ring currents (originating from reduction of oxygen traces) and normalized to the ring collection efficiency *N* and the number of electrons transferred in the oxygen reduction reaction (ORR) at the ring.

Figure 2. Carbon corrosion currents calculated from the corresponding RRDE transients shown in Fig. 1 and normalized to the: (a) geometric surface area; (b) residual mass of carbon materials; (c) residual surface area of carbon materials. Although partial exposure of the GC surface to the solution cannot be fully excluded, background GC correction was not applied in Fig. 2b and 2c, considering high loading (91 μg cm^{-2}) and even distribution of the carbon powders along the GC support. The residual carbon mass was calculated using Faraday's law assuming $4e^-$ carbon oxidation and neglecting surface passivation currents. The residual surface area of carbon materials was calculated from the initial BET surface area multiplied by the residual carbon mass.

Figure 3. Carbon corrosion currents (a-b) and corresponding lifetimes (c) plotted *vs.* anodic potentials and normalized to the: (a) residual mass of carbon materials; (b) residual surface area of carbon materials. The residual carbon mass was calculated using Faraday's law assuming $4e^-$ carbon oxidation and neglecting surface passivation currents. The residual surface area of carbon materials was calculated from the initial BET surface area multiplied by the residual carbon mass. Corrosion currents were taken at the end of each transient shown in Fig. 2 and in some cases did not reach steady-state values.

Figure 4. RRDE transients of GC-supported carbon materials and bare GC at 1600 rpm in N_2-saturated 1 M NaOH with loadings of 91 μg cm^{-2}_{geo} at 1.63 V and 5 h duration: (a) disk currents; (b) normalized ring currents at E_{Ring} = 0.3 V; (c) oxygen faradaic efficiency. A short polarization step at 0.93 V is applied before and after anodic polarization. Ring

currents are corrected to the background ring currents (originating from reduction of oxygen traces) and normalized to the ring collection efficiency *N* and number of electrons transferred in the oxygen reduction reaction (ORR) at the ring. Inset in the panel c represents the oxygen efficiency for the acetylene black recorded after the manual oxygen bubbles removal (see the main text for details).

Figure 5. Carbon corrosion currents calculated from the corresponding RRDE transients shown in Fig. 4 and normalized to the: (a) geometric surface area; (b) residual mass; and (c) residual surface area of carbon materials. The residual carbon mass was calculated using Faraday's law assuming 4e$^-$ carbon oxidation and neglecting surface passivation currents. The residual surface area of carbon materials was calculated from the initial BET surface area multiplied by the residual carbon mass. The dashed green curve represents the acetylene black oxidation current calculated assuming 95% oxygen efficiency during the whole duration of the anodic polarization (see the main text for details).

Figure 6. TEM images of acetylene black before (a) and after (b-d) anodic polarization performed at 1.63 V during 5 h in N_2-saturated 1 M NaOH without (a-c) and with (d) the addition of LMSC perovskite OER catalyst.

Figure 7. RRDE transients of GC-supported mixtures of $La_{0.5}Sr_{0.5}Mn_{0.5}Co_{0.5}O_{3-\delta}$ and various carbon materials, GC-supported $La_{0.5}Sr_{0.5}Mn_{0.5}Co_{0.5}O_{3-\delta}$ and bare GC at 1600 rpm in N_2-saturated 1 M NaOH with loadings of 15 μg cm^{-2}_{geo} for each component at 1.63 V and 5 h duration: (a) disk currents; (b) normalized ring currents at E_{Ring} = 0.3 V; (c) oxygen faradaic efficiency. A short polarization step at 0.93 V was applied before and after the anodic polarization. Ring currents are corrected to background ring currents (originating from reduction of oxygen traces) and normalized to the ring collection efficiency *N* and the number of electrons transferred in the oxygen reduction reaction (ORR) at the ring.

Figure 8. EDX elemental mapping of LSMC particles in the LSMC/Vulcan XC-72R composition after anodic polarization performed at 1.63 V in N_2-saturated 1 M NaOH during 5 h.

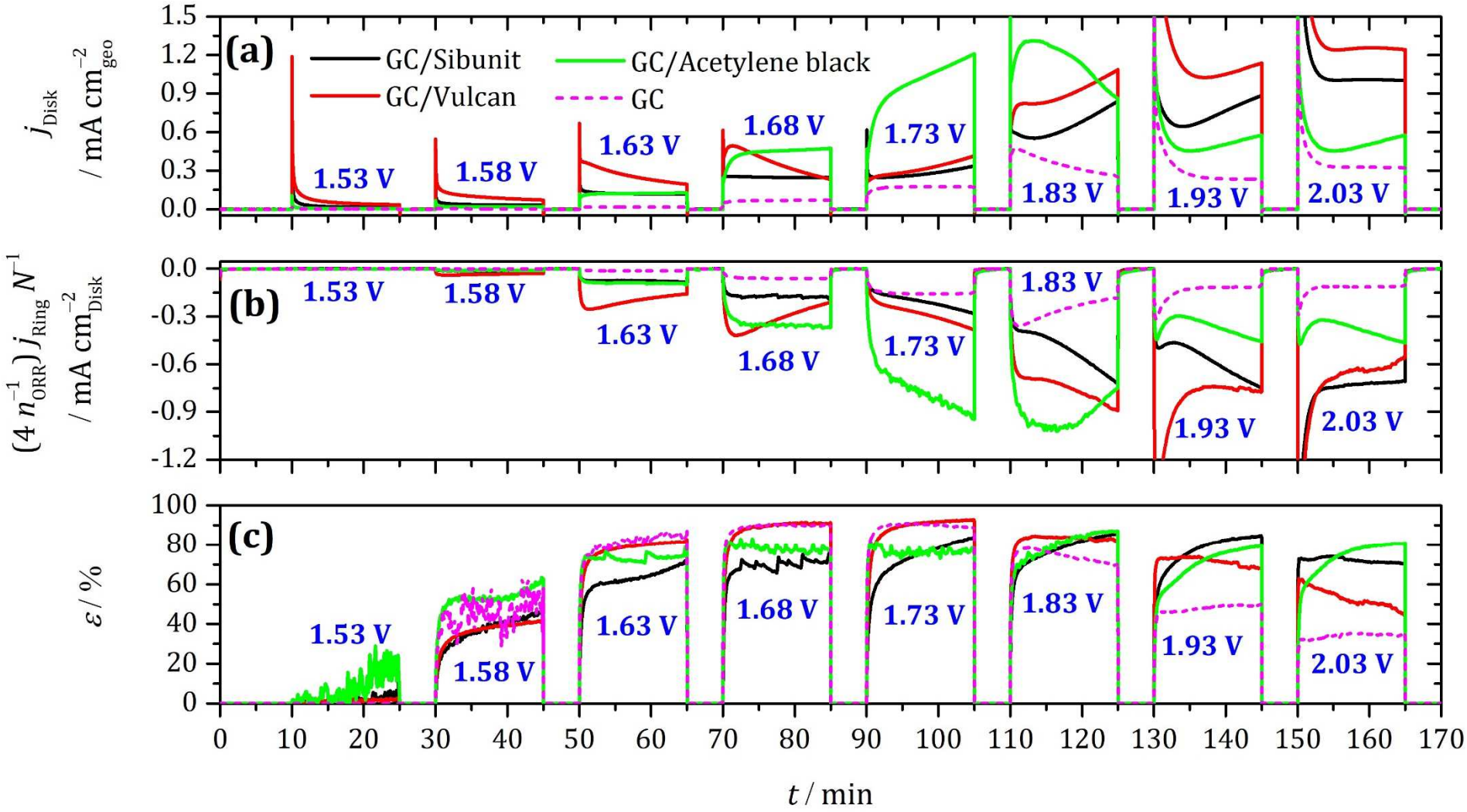
(a)
GC/Sibunit
GC/Vulcan
GC/Acetylene black
GC
1.53 V
1.58 V
1.63 V
1.68 V
1.73 V
1.83 V
1.93 V
2.03 V
j_{Disk} / mA cm$^{-2}_{geo}$
(b)
$(4\ n_{ORR}^{-1})\ j_{Ring}\ N^{-1}$ / mA cm$^{-2}_{Disk}$
(c)
ε / %
t / min

Figure 1.

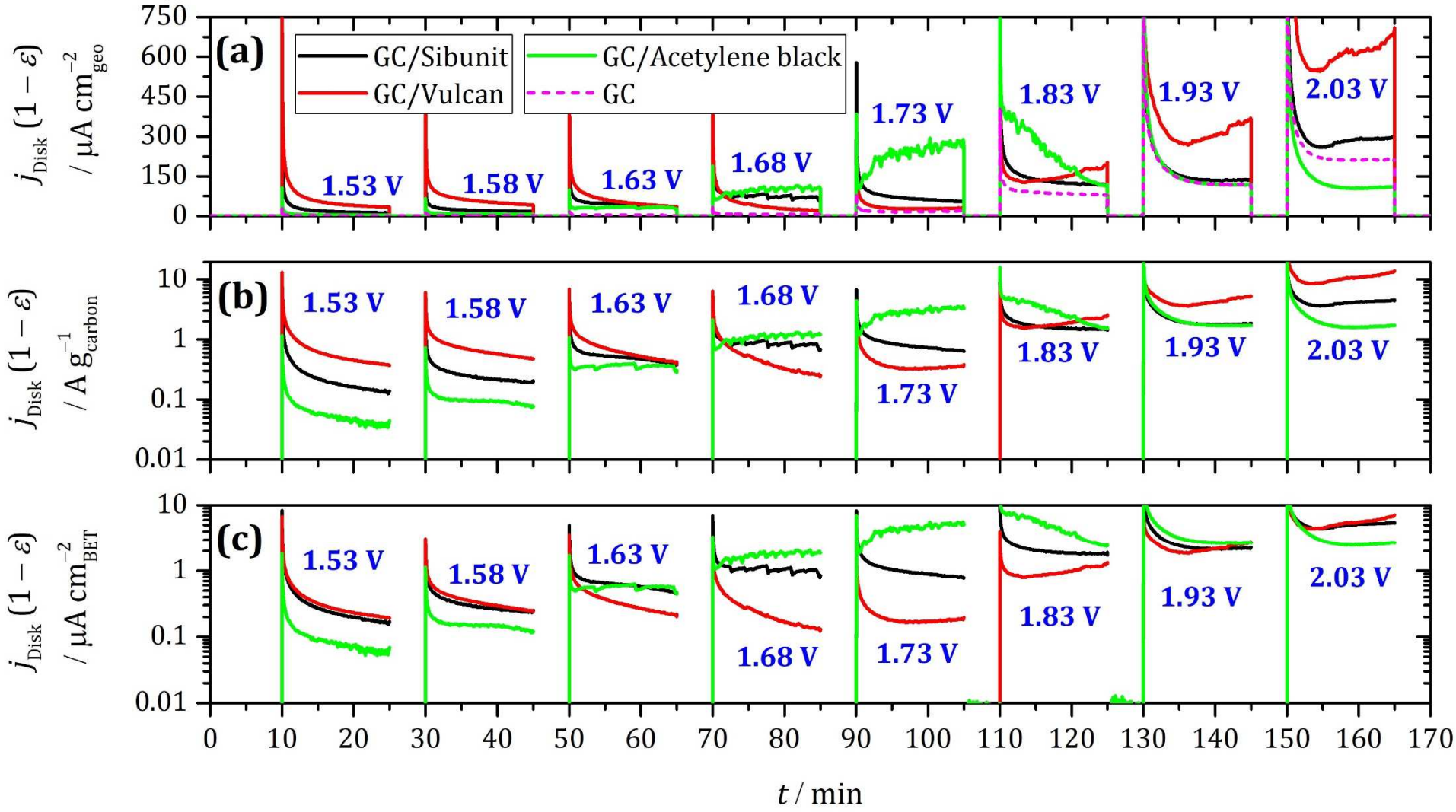
(a)
(b)
(c)
GC/Sibunit
GC/Vulcan
GC/Acetylene black
GC
1.53 V
1.58 V
1.63 V
1.68 V
1.73 V
1.83 V
1.93 V
2.03 V
$j_{Disk}\,(1-\varepsilon)$ / μA cm^{-2}_{geo}
$j_{Disk}\,(1-\varepsilon)$ / A g^{-1}_{carbon}
$j_{Disk}\,(1-\varepsilon)$ / μA cm^{-2}_{BET}
t / min

Figure 2.

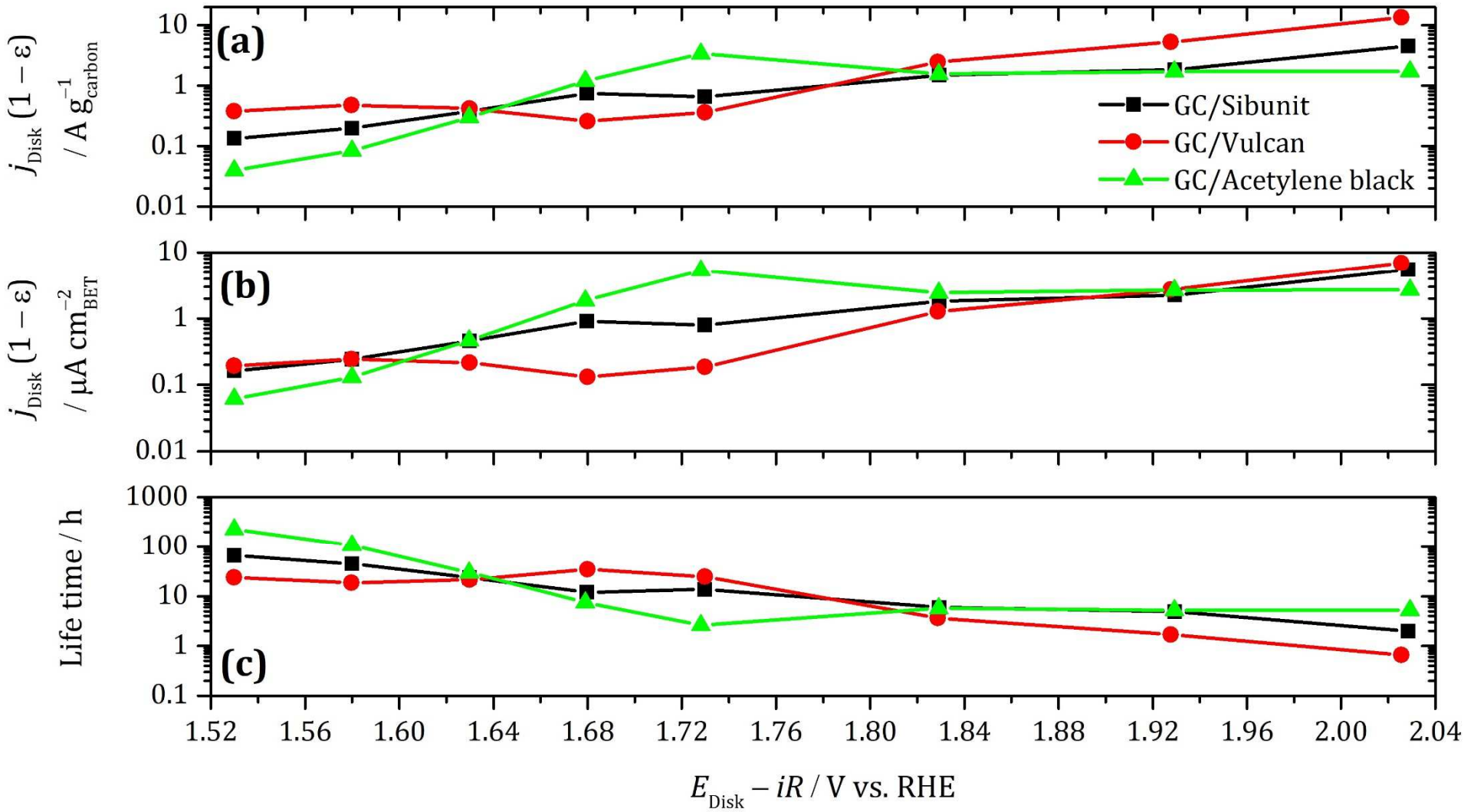
(a)
(b)
(c)
GC/Sibunit
GC/Vulcan
GC/Acetylene black
$j_{Disk}(1-\varepsilon)$ / A g_{carbon}^{-1}
$j_{Disk}(1-\varepsilon)$ / μA cm_{BET}^{-2}
Life time / h
10
1
0.1
0.01
1000
100
1.52
1.56
1.60
1.64
1.68
1.72
1.76
1.80
1.84
1.88
1.92
1.96
2.00
2.04
$E_{Disk} - iR$ / V vs. RHE

Figure 3.

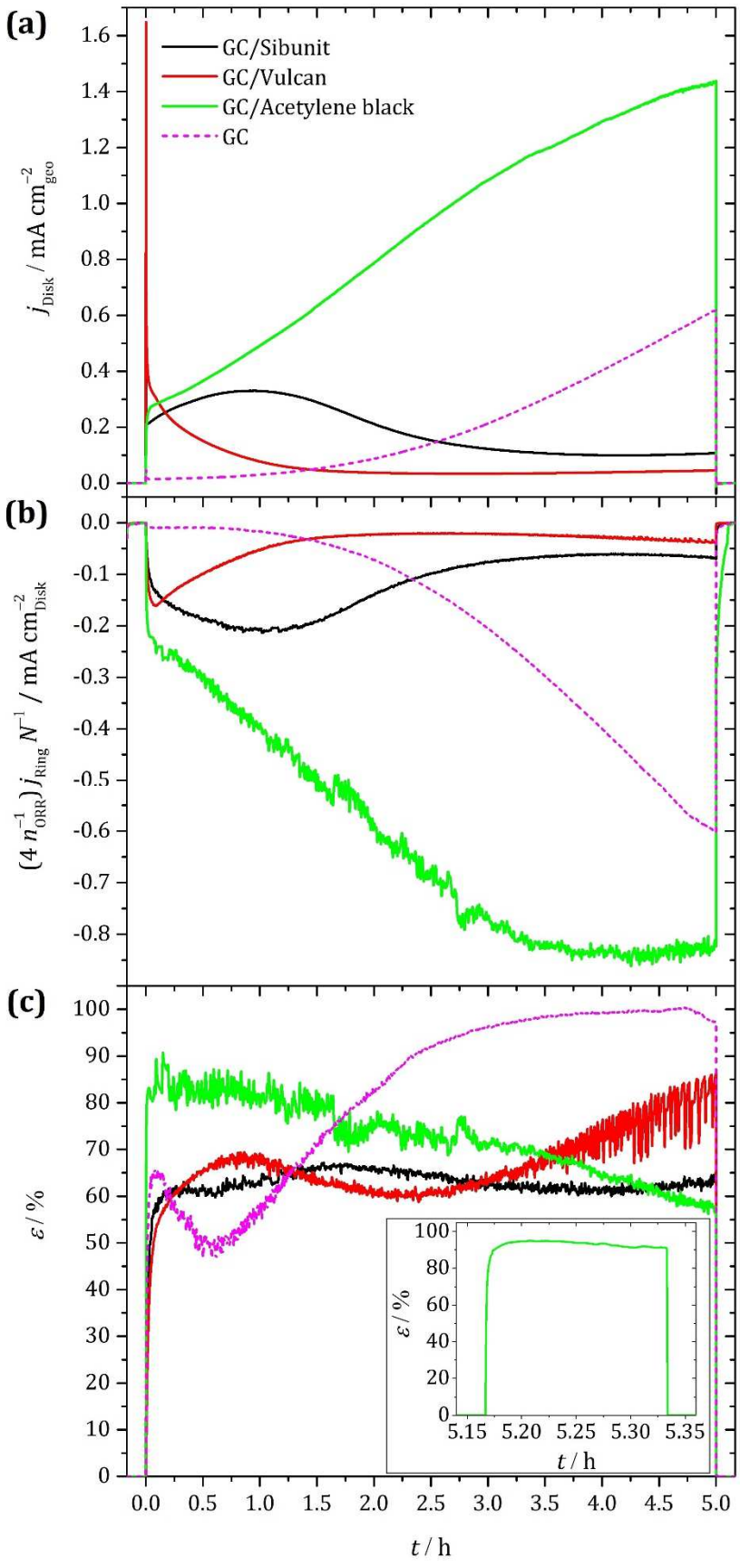
(a)
GC/Sibunit
GC/Vulcan
GC/Acetylene black
GC
j_{Disk} / mA cm$^{-2}_{geo}$
(b)
$(4\ n_{ORR}^{-1})\ j_{Ring}\ N^{-1}$ / mA cm$^{-2}_{Disk}$
(c)
ε / %
t / h
ε / %
t / h

Figure 4.

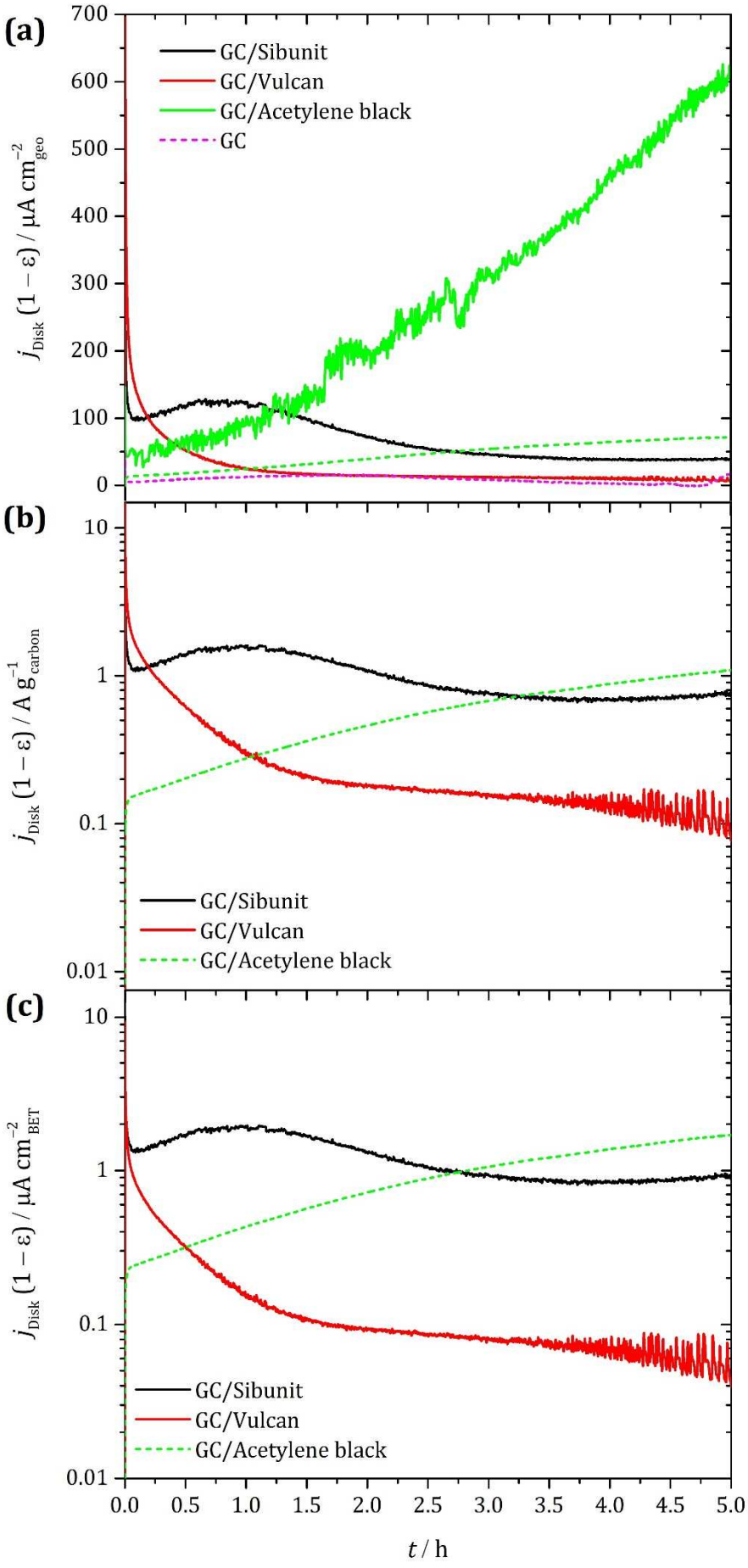
(a)
GC/Sibunit
GC/Vulcan
GC/Acetylene black
GC
$j_{Disk}\,(1-\varepsilon)$ / μA cm^{-2}_{geo}
(b)
$j_{Disk}\,(1-\varepsilon)$ / A g^{-1}_{carbon}
GC/Sibunit
GC/Vulcan
GC/Acetylene black
(c)
$j_{Disk}\,(1-\varepsilon)$ / μA cm^{-2}_{BET}
GC/Sibunit
GC/Vulcan
GC/Acetylene black
t / h

Figure 5.

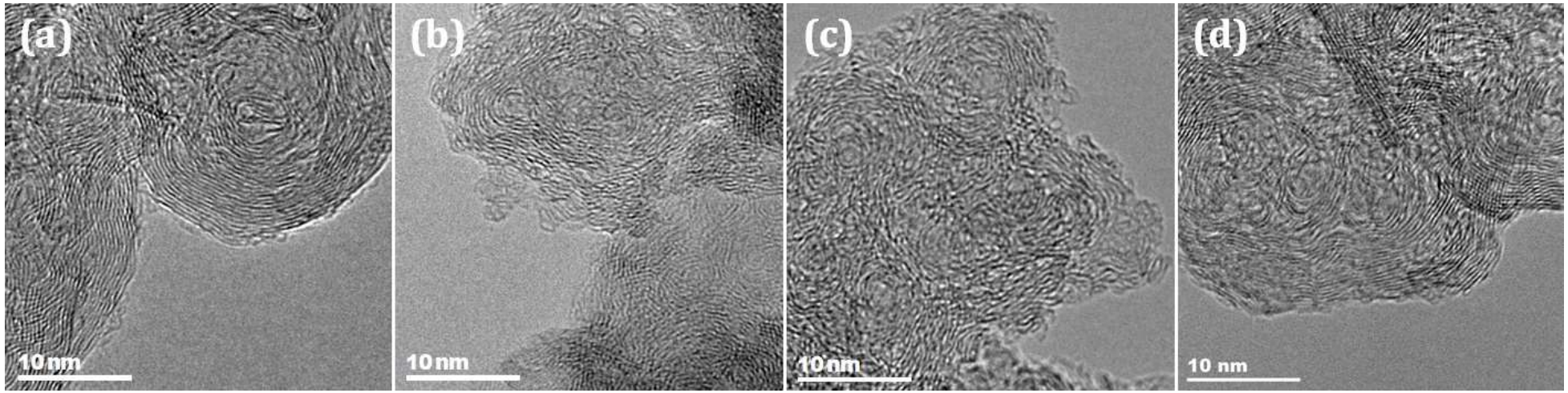

Figure 6.

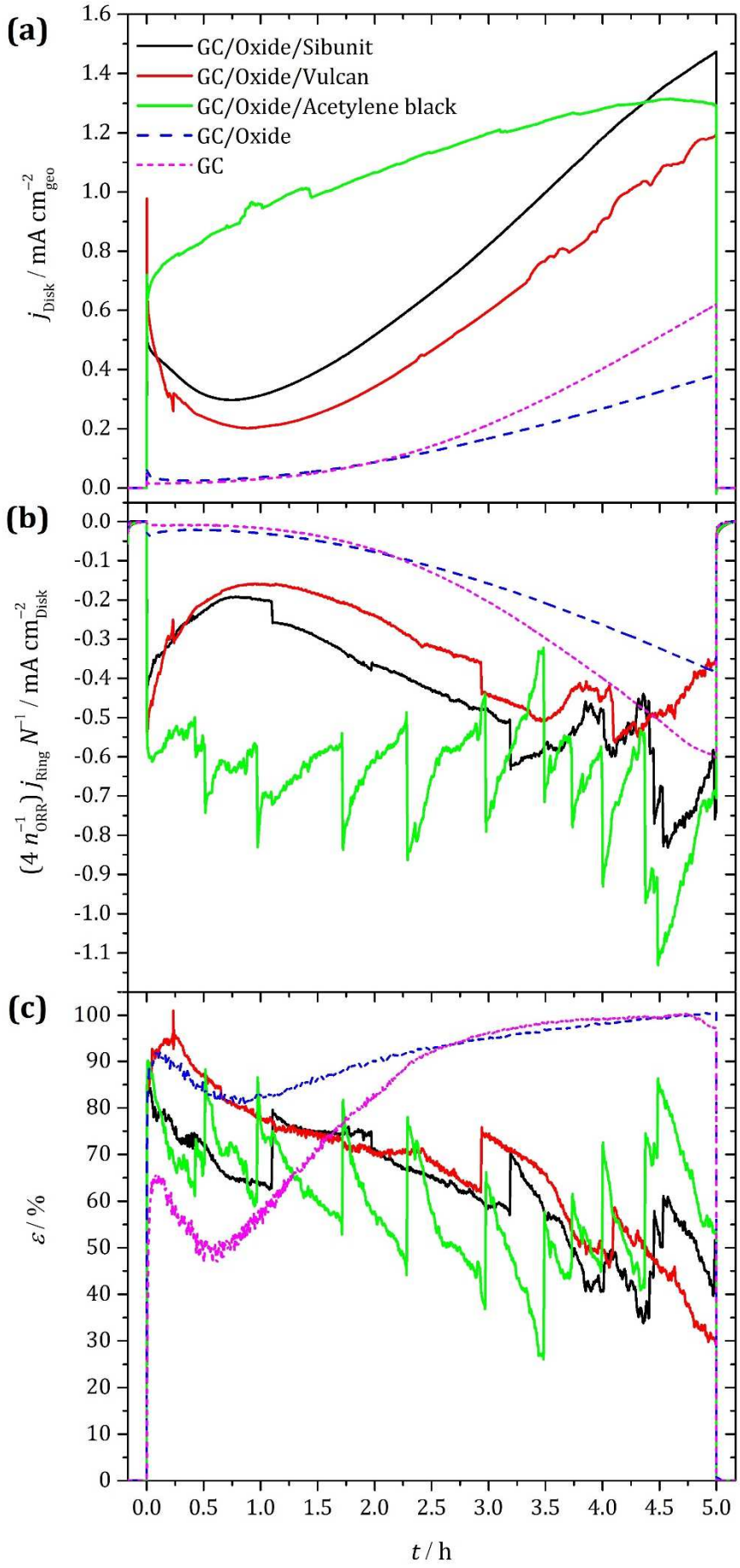
(a)
GC/Oxide/Sibunit
GC/Oxide/Vulcan
GC/Oxide/Acetylene black
GC/Oxide
GC
j_{Disk} / mA cm$^{-2}_{geo}$
(b)
$(4\ n^{-1}_{ORR})\ j_{Ring}\ N^{-1}$ / mA cm$^{-2}_{Disk}$
(c)
ε / %
t / h

Figure 7.

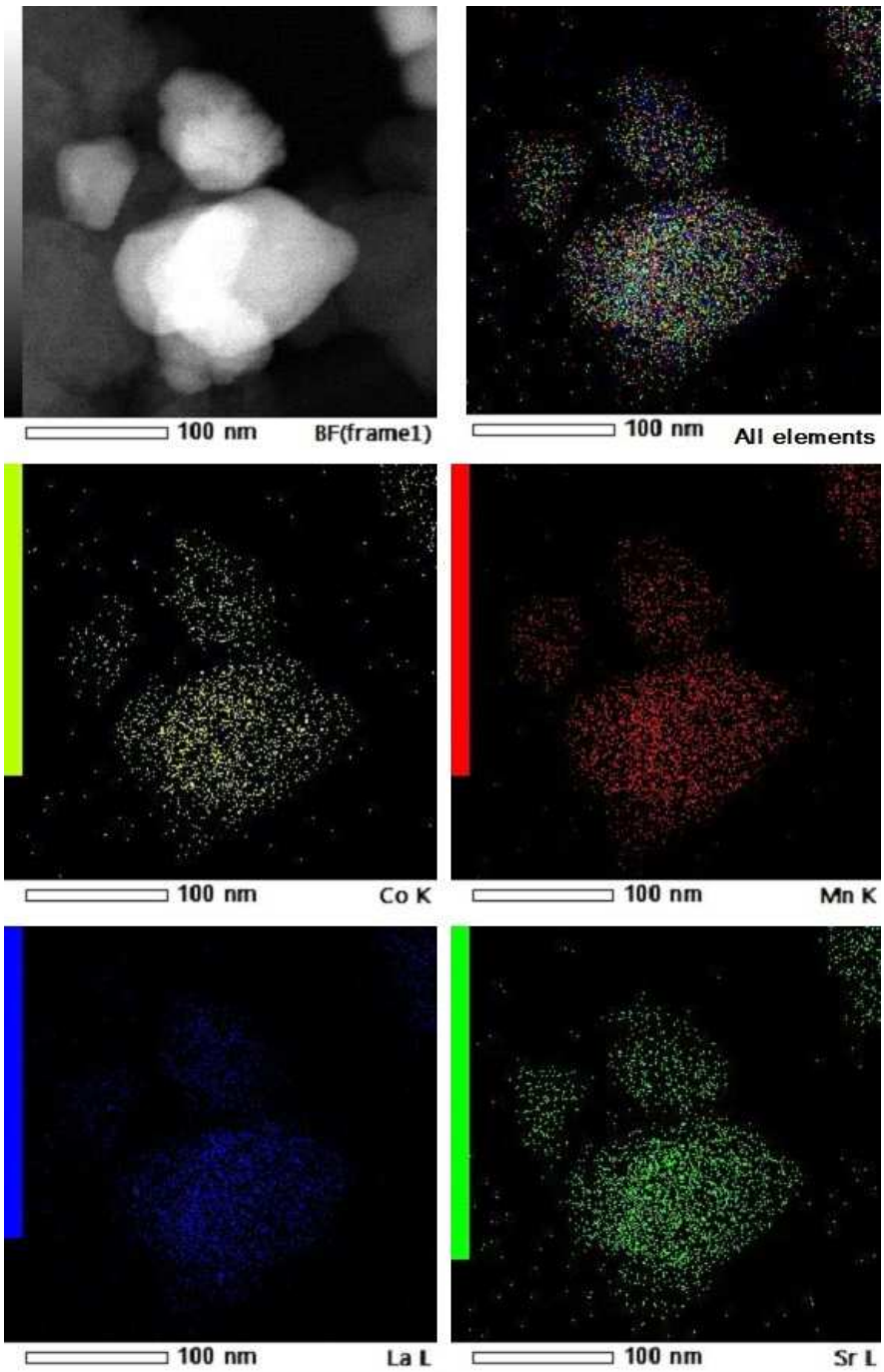
100 nm
BF(frame1)
100 nm
All elements
100 nm
Co K
100 nm
Mn K
100 nm
La L
100 nm
Sr L

Figure 8.

Table 1

Morphological, structural and electrochemical characteristics of carbon materials investigated in this work.

Carbon material	S_{BET}, $m^2\ g^{-1}$	S_{BJH}[a], $m^2\ g^{-1}$	S_{micro}[b], $m^2\ g^{-1}$	V_{micro}[b], $mm^3\ g^{-1}$	C_{BET}[c], $\mu F\ cm^{-2}$	C_{BJH}[d], $\mu F\ cm^{-2}$	Contact angle[e], °	θ basal planes		L_a[h], nm	L_b[h], nm	d_{002}[h], nm
								[f]	[g]			
Sibunit-152	82	79	19	10	6.6	6.9	50	0.55	0.62	2.7	2.5	0.355
Vulcan XC-72R	194	117	118	59	4.6	7.7	85	0.55	0.48	2.3	1.9	0.364
Acetylene black	64	47	~0	~0	2.1	2.9	140	0.76	0.79	2.9	3.0	0.352

[a] Surface area determined using the BJH method from the adsorption branch of the isotherm.
[b] Determined from N_2 adsorption data using *t*-plot.
[c] Calculated from CV (Fig. S1) charges in the 0.93 to 1.03 V potential window and normalized to the BET surface area.
[d] Calculated from CV (Fig. S1) charges in the 0.93 to 1.03 V potential window and normalized to the BJH surface area.
[e] Contact angle from Ref. [28].
[f] Basal plane coverage calculated from the $PdCl_2$ adsorption data in Ref. [29].
[g] Basal plane coverage calculated from pseudocapacitances in Ref. [28].
[h] Size of the X-ray coherent scattering domains and (002) interlayer spacing determined from powder diffraction data. These values are taken from Ref. [28] after a correction of certain misprints.